

## New Insights from Revisiting the Rotation Period of the Strongly Magnetic O Star, NGC 1624-2

S. SEADROW,<sup>1</sup> V. PETIT,<sup>1</sup> G. A. WADE,<sup>2,3</sup> D. BOHLENDER,<sup>4</sup> J. MAÍZ APELLÁNIZ,<sup>5</sup> A. DAVID-URAZ,<sup>6</sup> M. OKSALA,<sup>7,8</sup> AND J. MACDONALD<sup>1</sup>

<sup>1</sup>*Department of Physics & Astronomy, Bartol Research Institute, University of Delaware, Newark, DE, 19714, USA*

<sup>2</sup>*Department of Physics, Engineering Physics & Astronomy, Queen's University, Kingston, Ontario K7L 3N6, Canada*

<sup>3</sup>*Department of Physics & Space Science, Royal Military College of Canada, PO Box 17000, Station Forces, Kingston, ON K7K 7B4, Canada*

<sup>4</sup>*Dominion Astrophysical Observatory, Herzberg Astronomy and Astrophysics Program, National Research Council of Canada  
5071 West Saanich Road, Victoria, BC V9E 2E7, Canada*

<sup>5</sup>*Centro de Astrobiología (CAB), CSIC-INTA, Campus ESAC. C. Bajo Del Castillo S/N, E-28 692 Madrid, Spain*

<sup>6</sup>*Department of Physics, Central Michigan University, Mount Pleasant, MI, 48859, USA*

<sup>7</sup>*Department of Physics, California Lutheran University, Thousand Oaks, CA, 91360, USA*

<sup>8</sup>*LESIA, Paris Observatory, PSL University, CNRS, Sorbonne University, Université Paris Cité, 5 place Jules Janssen, Meudon, France*

(Accepted February 9, 2026)

Submitted to ApJ

### ABSTRACT

NGC 1624-2 hosts the strongest surface magnetic field found on an O star thus far. When applied across several epochs of observations, the star's currently accepted rotation period (157.99 d) does not coherently characterize the variations of spectral lines of magnetospheric origin. We analyze Lomb-Scargle periodograms produced with new and archival, multi-instrument spectroscopic time series of Balmer H and He spectral lines. We find that  $153.17 \pm 0.42$  d and  $306.56 \pm 1.19$  d are both equally suitable periods at phasing the spectral and magnetic time series data in a manner consistent with the Oblique Rotator Model. The 306.56 d period implies a magnetic geometry for NGC 1624-2 that is quite different from the previously accepted one, for which both magnetic poles should be observed during a full rotational cycle. If this is the case, the star's magnetic South pole has yet to be observed, and additional spectropolarimetric observations should be acquired in order to confirm whether or not the south pole is in fact observable.

**Keywords:** Massive stars (772) — Stellar magnetic fields (1610) — Stellar rotation (1629) — O stars(1137) — Lomb-Scargle periodogram(1959) — Spectropolarimetry(1973) — Spectroscopy(1558)

### 1. INTRODUCTION

An estimated 7% of Galactic O stars possess detectable surface magnetic fields (Grunhut et al. 2017). These fields are organized (predominantly large-scale dipoles), strong (1 to 10 kG), and stable. Currently, the mechanism generating these fields is poorly understood. The leading hypothesis suggests that these fields are of fossil origin: the magnetic fields are either byproducts of main-sequence star mergers or remnants of the Interstellar Medium's magnetism. (see e.g. Keszthelyi 2023, for a recent review). Their origins notwithstanding, magnetic O stars serve as laboratories to test the dynamical

interactions of large-scale, surface magnetic fields with stellar properties such as rotation and mass loss (e.g. ud-Doula et al. 2008; Meynet et al. 2011; Petit et al. 2017).

NGC 1624-2, a main-sequence O7f?p star, hosts the strongest known magnetic field found on a main-sequence O star. Its magnetic field is measured to be  $\sim 20$ kG (Wade et al. 2012a, hereafter W12), roughly an order of magnitude stronger than the other magnetic O stars<sup>1</sup>. This star provides the opportunity to explore strong magnetic field effects in the high-mass regime.

<sup>1</sup> We specify *main-sequence* magnetic O stars because the recently discovered 40 kG, magnetic quasi-Wolf-Rayet star, HD 45166, exhibits O-type spectral features and the rare O?p peculiarity (Shenar et al. 2023). However, as a stripped  $\sim 2M_{\odot}$  star, its initial magnetic and stellar evolution remains uncertain.

Corresponding author: Shaquann Seadrow  
 sseadrow@udel.edu

In this paper, we present evidence that either i) the rotational period of NGC 1624-2 needs to be revised downwards by a few days, affecting the phasing of recent observations, or ii) the rotational period of NGC 1624-2 is, in fact, twice as long as originally reported, with significant consequences for the geometry of the magnetic field.

### 1.1. Background on the ORM and magnetosphere model

Rotation periods of most magnetic massive stars can be measured by exploiting the misalignment between the magnetic field and the rotational axis (by an angle  $\beta$  known as the *obliquity*). As long as the star's rotation axis is also tilted (by an *inclination* angle  $i$ ) with respect to the line of sight, our view of the surface field changes as the star rotates. Therefore, magnetic field measurements like the mean longitudinal field ( $\langle B_z \rangle$ ) and the mean magnetic modulus ( $\langle B \rangle$ ) will vary periodically<sup>2</sup>. This is referred to as the Oblique Rotator Model (ORM; [Stibbs 1950](#)).

For some stars, the mean modulus can be measured using the Zeeman splitting that is seen directly in their spectra (e.g. [Mathys 2017](#)). However, massive stars have other competing line-broadening mechanisms, so they are rarely observed. Instead, the variation of  $\langle B_z \rangle$  is usually studied, but this requires spectropolarimetric observations to measure the change in circular polarization (Stokes  $V$ ) across the line profiles ([Donati et al. 1997](#)).

Alternatively, some rotation periods of magnetic massive stars can be measured using only spectroscopy. Strong magnetic fields will channel and confine the stars' ionized, radiatively-driven winds into circumstellar *magnetospheres* with associated emission. These magnetospheric boundaries, characterized by the Alfvén radii, can extend multiple times the stellar radius ([ud-Doula & Owocki 2002](#); [ud-Doula et al. 2008, 2009](#)). For stars without dynamically significant rotation, which is common for magnetic O stars, the wind material becomes highly concentrated around the magnetic equator. For tilted magnetic fields, emission from the magnetosphere, such as  $H\alpha$ , is variable and rotationally modulated ([Owocki et al. 2016](#)). Though spectroscopy of magnetospheric emission is more convenient than spectropolarimetry in measuring rotation rates, it bears the disadvantage of not being sensitive to magnetic field polarity.

We often establish a clock around the time of maximum and minimum magnetospheric emission, which are referred to as "high state" and "low state", respectively (e.g. [Nazé et al. 2007](#)). A high state in magnetospheric emission occurs when the magnetic axis, *regardless of polarity*, is as close as possible to the line of sight, so that the bulk of the dense

magnetospheric material (tracing more or less the magnetic equator) is seen as close to face-on as possible. A high state coincides with an extremum (the non-zero absolute maximum or minimum) of the longitudinal magnetic field. A low state in magnetospheric emission occurs when the bulk of the dense magnetospheric material is seen as close to edge-on as possible; this means that the magnetic equator will be as close as possible to our line of sight. Depending on whether or not the longitudinal field curve crosses zero, the associated longitudinal magnetic field will either be zero or values close to zero.

For predominantly dipolar magnetic fields, magnetospheric emission cycles exhibit either single-wave or double-wave variation.

- Single-wave variation arises from a geometry in which only one magnetic pole (North or South) comes into view over the course of the rotation cycle. We will only see one high state per rotation, and generally, the longitudinal field curve does not cross zero but rather remains consistently positive or negative. At most, the hidden pole will appear at the limb of the stellar disk, in which case the minimum of the longitudinal field curve reaches zero.
- Double-wave variation arises from a geometry in which both poles will come into view over the course of the rotation cycle. We will see two (potentially unequal) maxima of emission (high states) per rotation, and the longitudinal field curve crosses zero twice per rotation. One high state will coincide with the positive extremum of the longitudinal magnetic field curve, and one will coincide with the negative extremum; as with their high states, the North and South longitudinal magnetic field measurements can potentially be unequal in magnitude.

However, determining the rotation period solely by magnetospheric emission can lead to ambiguity in the inferred magnetic geometry, such as when double-wave variations have identical high state amplitudes. Thus, magnetic measurements can lift this degeneracy.

### 1.2. Previous studies of NGC 1624-2

The magnetic field of NGC 1624-2 was first detected by [W12](#) using spectropolarimetric observations taken at two epochs. Strong Stokes  $V$  signatures were present in multiple spectral lines, and the associated maximum  $\langle B_z \rangle$  was 5.4 kG. Additionally, it is the only magnetic O star to have Zeeman splitting observed in its spectra, specifically  $CIV \lambda 5801$  and  $CIV \lambda 5812$ . That Zeeman splitting yielded  $\langle B \rangle \sim 14$  kG (maximum value). With only two measurements to apply the ORM to, their estimated  $\sim 20$  kG dipolar field strength is a lower limit.

<sup>2</sup>  $\langle B_z \rangle$  is the brightness-weighted longitudinal component of the surface field averaged over the stellar disk.  $\langle B \rangle$  is the brightness-weighted magnitude of the surface field averaged over the stellar disk.

[W12](#) estimated the extent of the magnetosphere, using the formulation of [ud-Doula & Owocki \(2002\)](#), to be around  $10R_\star$  and they indeed noted many rotationally modulated emission lines. They used a large sample of spectroscopic observations to measure the equivalent widths of these emission lines and inferred a rotational period of 157.99 d that produced a single-wave variation. We note that as there were only two spectropolarimetric observations at the time, the longitudinal field measurements were not used to determine this period. That said, the two positive  $\langle B_z \rangle$  measurements were compatible with the proposed single-wave magnetic geometry.

[David-Uraz et al. \(2021, hereafter DU2021\)](#) and [Järvinen et al. \(2021, hereafter J2021\)](#) conducted spectropolarimetric follow-up studies of NGC 1624-2 with the same dataset, though using different methods. Their set of ESPaDOnS (CFHT) spectropolarimetric Stokes  $V$  observations spans 3 years ( $\sim 8$  completed rotations since HJD<sub>0</sub>) and has even phase coverage when phased with the 157.99 d period of [W12](#). Both studies evaluate the variations of  $\langle B_z \rangle$  and  $\langle B \rangle$  time series, but [DU2021](#) used the FWHM of CIV $\lambda 5812$  as a proxy for  $\langle B \rangle$  while [J2021](#) derived  $\langle B \rangle$  from the splitting of CIV $\lambda 5812$ . All of the longitudinal field measurements were positive and phased well with the 157.99 period. Therefore, neither study explored alternative periods nor magnetic geometries. That said, both studies arrived at the same conclusion that the field potentially has a topology more complex than a single dipole, given that  $\langle B \rangle$  unexpectedly reaches a maximum (rather than a minimum) at the same phase at which  $\langle B_z \rangle$  reaches its minimum.

[DU2021](#) conducted a follow-up UV spectroscopic study (to [David-Uraz et al. \(2019\)](#)) of NGC 1624-2 as well. [DU2021](#) reported that the wind-sensitive resonance lines exhibit three apparent high states within a full rotation. They hypothesized that this could be a consequence of a slight inaccuracy in the 157.99 d rotation period, as the UV observations were obtained at a later epoch than the optical spectra of [W12](#) and their available spectropolarimetric observations. Thus in this paper, we will first demonstrate that new spectroscopic observations indeed show that the rotational period needs to be revised.

We will also demonstrate that a longer double-wave period of the order of 300 d is perfectly compatible with all existing magnetic and magnetospheric observations. [W12](#) ruled out a double-wave variation of magnetospheric emission lines, but their conclusion assumed that maxima should be unequal (for an example, see the H $\alpha$  EW variation of  $\sigma$  Ori E in Figure 4 of [Oksala et al. 2012](#)). Therefore, a double-wave variation with comparable or equal maxima cannot be ruled out, as we will show. Unfortunately, the possibility of a double-wave variation and a longer  $\sim 300$  d period was never considered in any study thus far; all magnetospheric or spectropolarimetric studies have solely relied on the 157.99 d period.

We present our observations and data reductions in §2, and demonstrate that new magnetospheric spectroscopic observations do not phase well with the 157.99 d period in §3. We present our period determination method in §4. We present our results for single-wave periods in §5.1 and our results for double-wave periods in §5.2. We discuss the implications of our results on the inferred magnetic geometry (§6.1) and the impact of our results on previous studies of NGC 1624-2 (§6.2). We summarize our conclusions in §6.3.

## 2. OBSERVATIONS

We use a collection of optical spectra from spectroscopic and spectropolarimetric observations (the full log of observations can be found in Table A1).

*ESPaDOnS and NARVAL* : We use the Stokes  $I$  (unpolarized) spectra of 23 archival optical spectropolarimetric observations obtained with the Echelle SpectroPolarimetric Device for the Observation of Stars (ESPaDOnS) mounted on the Canada-France-Hawaii Telescope (CFHT) and its twin instrument Narval at the Télescope Bernard Lyot. These observations were obtained mostly between September 2012 and November 2013, with an additional observation in September 2015. These are high-spectral-resolution observations ( $R=65,000$ ) that provide a wavelength coverage from  $\sim 370$  nm to 1050 nm. The first two observations were key to the initial magnetic field analysis of NGC 1624-2 by [W12](#), and the full set of spectropolarimetric observations was used in the recent magnetic geometry analyses of [DU2021](#) and [J2021](#).

We use optical spectroscopy from the Library of Libraries of Massive-Star High-Resolution Spectra project (LiLiMaRlin; [Maíz Apellániz et al. 2019a](#)), which has an extensive collection of archival optical spectra. We include the following datasets:

*NoMaDs*: We use the same spectroscopic observations ( $R=30,000$ ) from the NoMaDs Project ([Maíz Apellániz et al. 2012](#)) that were used in the period analysis of [W12](#). These observations were obtained between 2011 and 2012 with the HRS spectrograph on the Hobby Eberly Telescope (9.2 m) at the McDonald Observatory. For our analysis, we use observations with the B (wavelength range of  $\sim 380$  to 470 nm), V ( $\sim 530$  to 630 nm), and R ( $\sim 640$  to 730 nm) configurations.

*HERMES*: We use 2 high-resolution spectra gathered with the High Efficiency and Resolution Mercator Echelle Spectrograph (HERMES;  $R=85,000$ ) on the Mercator telescope (1.2 m) at the Observatorio del Roque de Los Muchachos. These observations were obtained in October 2016 and 2017 and provide a wavelength coverage of  $\sim 370$  nm to 900 nm.

*FIES*: We use observations obtained with the FIbre-fed Échelle Spectrograph (FIES) aboard the Nordic Optical Telescope at the ORM. These observations are made available in the OB star spectroscopic database from the IACOB project ([Simón-Díaz et al. 2015, 2020](#)). We use 4 observations, one

obtained with the FIES high resolution mode ( $R=67,000$ ) and 3 with the lower resolution mode ( $R=25,000$ ). These observations were taken between November 2017 and October 2019 and provide a wavelength range of  $\sim 370$  nm to 900 nm.

**CAFÉ-BEANS:** We use four high-resolution ( $R=65,000$ ) observations from the CAFÉ-BEANS (CAFÉ-Binary Evolution Andalusian Northern Survey) survey (Negueruela et al. 2015). This survey obtained observations from the Calar Alto Fiber-fed Échelle spectrograph (CAFÉ) on the 2.2m telescope at the Calar Alto Observatory between October 2012 and January 2014. The observations provide a wavelength coverage from  $\sim 360$  nm to 920 nm.

**DAO:** We use spectra obtained with the SITE-2 Cassegrain Spectrograph mounted on the 1.8m telescope at the Dominion Astrophysical Observatory (DAO), taken between November 2019 and February 2022. These  $R=15,700$  observations are centered on the rest wavelength of the  $\text{He I } \lambda 5876$  line, with coverage from 574 nm to 600 nm.

For the ESPaDOnS and DAO observations, we co-add the spectra that were acquired in a single observing night and use their mean HJDs. Overall, we have a multi-epoch collection of observations for time series analyses.

### 3. EVIDENCE FOR THE NEED OF A NEW PERIOD

In Figure 1, we show the phase evolution of the  $\text{He I } \lambda 5876$  profiles when folded with a 157.99 d period (the 3 panels correspond to separate 3 epochs). We calculate the phase using the ephemeris reported by W12,

$$\text{HJD} = 2455967.0 + 157.99 \times E. \quad (1)$$

In Equation 1, HJD is the Heliocentric Julian Date of the observation, the ‘time-zero’ Julian Date ( $\text{HJD}_0$ ) is  $2455967.0 \pm 10.0$  (the  $\text{HJD}_0$  uncertainty represents the phase-shift added to align a high state with  $\phi = 0$ ), the rotational period (denoted by the variable  $P$ ) is  $157.99 \pm 0.94$  d, and  $E$  is the sum of the rotation number and phase. We calculate the phase uncertainty using conventional error propagation while using the uncertainties in  $P$ . As seen in the left panel of the figure (the first few rotation cycles around the magnetic field detection),  $\text{He I } \lambda 5876$  profiles transition from emission (at high state) to a complex morphology with partial emission (at low state) and then back to emission. At later epochs (right panel), the profiles no longer vary smoothly with their adopted phases. At these later rotation cycles, the complex line morphologies share the same phases as the emission profiles at earlier epochs. This demonstrates the need to revise the rotational period of NGC 1624-2.

### 4. METHODS

Our objective is to determine the rotational period of NGC 1624-2 by examining the periodic variability of magnetospheric spectral lines. Following the method of W12, we use

the line profiles of  $\text{He I } \lambda 5876$ ,  $\text{He II } \lambda 4686$ ,  $\text{H}\alpha$ , and  $\text{H}\beta$  from the observations discussed in Section 2 and separately characterize their periodic variability with Lomb-Scargle (LS; Lomb 1976; Scargle 1982) periodograms. We use the LS periodogram because it is well-suited for time series with uneven and sparse sampling.  $\text{He I } \lambda 5876$  is the only line of the four that transitions into a complex morphology (hence why we chose it for visual displays); the others are consistently broad emission lines with variable intensities.

We apply the Lomb-Scargle method to time series of equivalent width (EW). We will first introduce the general preparations of the data for this method. We will then discuss the relevant details and considerations in the LS periodogram analyses.

The ESPaDOnS and NARVAL observations were normalized by MacInnis (2016). For the ESPaDOnS and NARVAL observations, the  $\text{H}\alpha$  and  $\text{H}\beta$  spectral lines lie in the overlapping regions of neighboring spectral orders. We use the upper order for  $\text{H}\alpha$  and the lower order for  $\text{H}\beta$ . Prior to co-addition, we use a 3rd-order polynomial fit of the continuum of each observation to normalize them. The remaining observations from the LiLiMaRlin project (Maíz Apellániz et al. 2019a) were already normalized.

We use the uncertainty-weighted implementations of LS, but the ESPaDOnS and NARVAL observations are the only ones that have pre-calculated flux error bars. We therefore measure the standard deviation of the normalized continuum and use it as a uniform uncertainty across all points on the line profile. To identify the continuum, we clip everything outside  $5\sigma$  ( $\sigma$  is the standard deviation of the full spectrum) and then apply a  $2\sigma$  clip for the LiLiMaRlin observations. We apply the same initial sigma-clip to the DAO observations and use  $3\sigma$  for the second clipping.

For each spectral line, we convert wavelengths to Doppler velocities and shift to NGC 1624-2’s rest frame using its 34 km/s radial velocity (Grunhut et al. 2017). For each spectral line, we apply an additional local normalization using a linear fit on points selected from the continuum on each side of the spectral lines.

Using the locally normalized line profiles, we calculate the equivalent widths in velocity units. We use an integration range with symmetric bounds about  $v = 0$ . We set the integration limits at 280, 300, 500, and  $250 \text{ km s}^{-1}$  for  $\text{He II } \lambda 4686$   $\text{He I } \lambda 5876$   $\text{H}\alpha$  and  $\text{H}\beta$  respectively. For the error bar calculation, we treat the integration as a right-handed Riemann approximation and apply conventional uncertainty propagation.

We analyze the variation of each equivalent width time series using LS periodograms (Lomb 1976) computed with astropy (Astropy Collaboration et al. 2013, 2018, 2022). Our grid of test periods, ranging from 10 d to 350 d, is uniformly spaced with  $\Delta P = 0.01$  d. Following standard

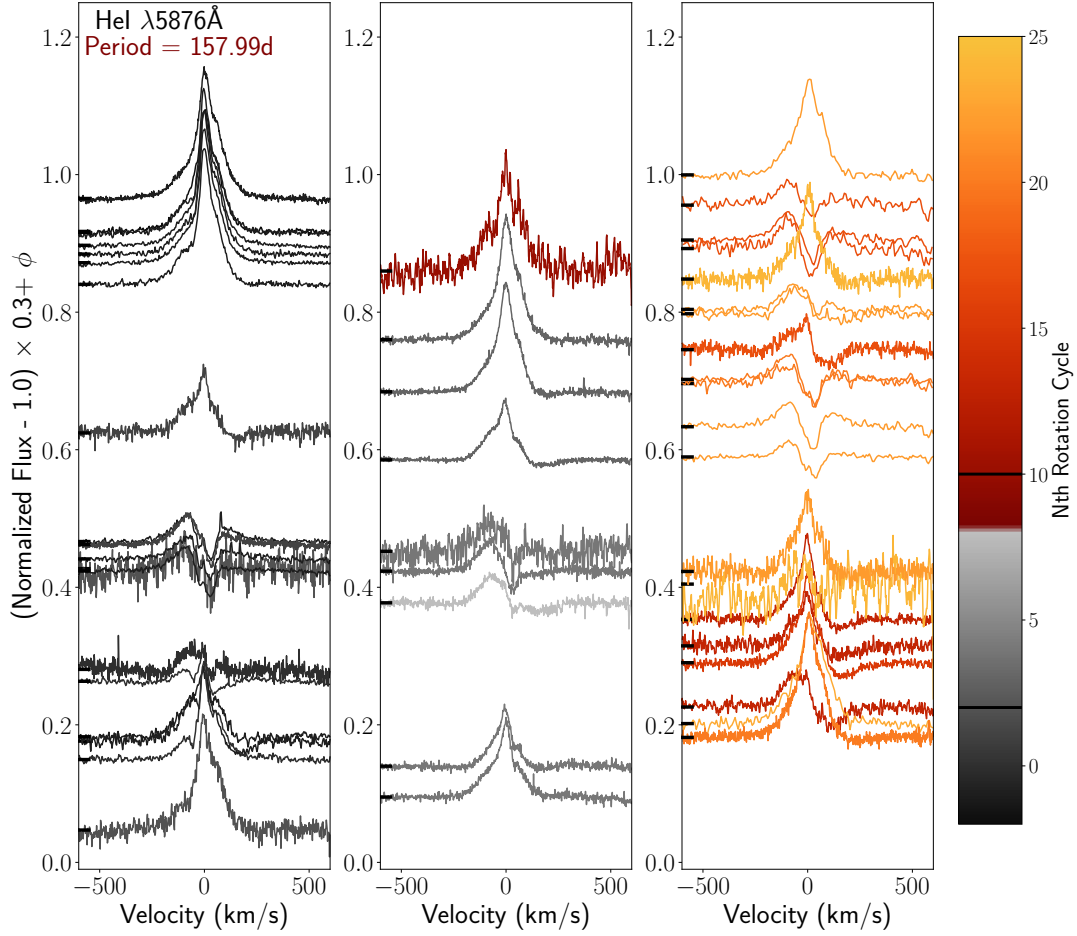


**Figure 1.** The He I  $\lambda 5876$  line profile variability. These normalized line profiles are plotted as a function of velocity in the stellar rest frame, scaled by 0.3, and shifted vertically according to their rotational phases using the ephemeris of W12 (the black dashes on the left are aligned with their continuum). The profiles are colored by their rotation number ( $N_{\text{rot}}$ ). The profiles are split among the left, center, and right panels by  $N_{\text{rot}} < 2$ ,  $2 \leq N_{\text{rot}} < 10$ , and  $N_{\text{rot}} \geq 10$ , respectively (also indicated by the black lines on the color bar). For display purposes, the MERCATOR observations were smoothed with a 7 point boxcar averaging.

considerations (VanderPlas 2018), this grid does not go below twice the shortest time interval between 2 consecutive EW measurements (effectively an approximation of the Nyquist Frequency when inverted), nor does it go above the total temporal length of each time series. We find that the minimum testable periods are 1.99 d, 1.87 d, 9.12 d, and 1.99 d for He II  $\lambda 4686$  He I  $\lambda 5876$  H $\alpha$  and H $\beta$  respectively.

The astropy LS algorithm allows us to manage the complexity of the model, which is defined as:

$$y(t; f) = \theta_0 + \sum_{n=1}^N [\theta_{2n-1} \sin(2\pi n f t) + \theta_{2n} \cos(2\pi n f t)]. \quad (2)$$

In this model, the free parameters are: the midline  $\theta_0$  (we use the mean EWs of each time series) and the amplitudes  $\theta_{2n-1}$  and  $\theta_{2n}$ . The 1-term model ( $N = 1$ ) would be a simple sinusoidal curve, and using high-order Fourier series would mean progressively adding sinusoids with harmonic frequencies.

We compute both 1-term and 2-term LS periodograms. We provide an example of these periodograms for the He II  $\lambda 4686$  time series in Figure 2(a). In the periodograms, we identify the peak with the highest power and verify that the peak is above the level at which the False Alarm Probability (FAP) is at most 0.005 (indicated by the gray dashed line)<sup>3</sup>. We calculate the FAP's via the bootstrap implementation in astropy's Lomb-Scargle function, but only for the 1-term LS (neither bootstrap nor analytical FAP estimates are available for the 2-term LS method). The bootstrap method randomly samples the EWs while keeping the original timestamps and computes a distribution of LS periodograms. Cloutier et al. (2018) states that "the bootstrap produces the most robust estimate of the FAP because it makes few assumptions about the form

<sup>3</sup> The FAP quantifies the probability that a peak would occur at or above a certain threshold, given the null hypothesis that the time series is not periodic. Peaks with high FAP are likely spurious.

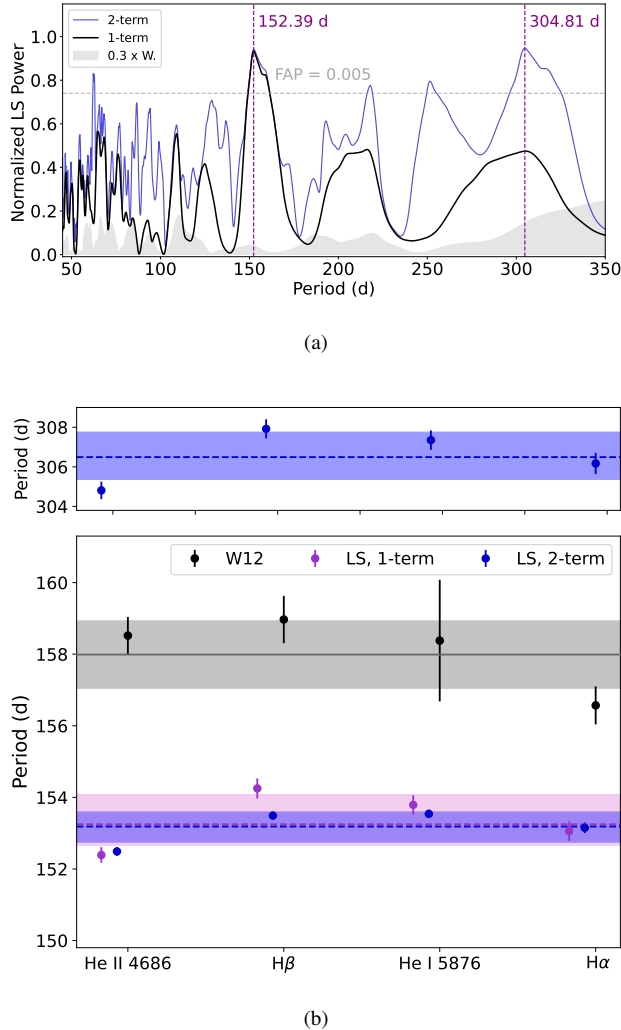


**Figure 2.** a) Periodograms from the  $\text{He II } \lambda 4686$  time series. The dashed gray line indicates the power above which the False Alarm Probability is below 0.005 for the 1-term LS only. We also show the window spectrum scaled by a factor of 0.3 in gray. We display the periodograms as a function of period to be consistent with Figure 5 of W12. b) Significant periods identified in the periodogram of the four spectral lines. The black points are measurements from the W12. The dark gray line and shaded area represent the original  $157.99 \pm 0.94$  d period. The purple and blue points are our 1-term and 2-term Lomb-Scargle (LS) derived periods, respectively. The dashed lines and shaded areas show the standard mean of the periods and their associated standard deviations.

of the periodogram distribution and fully accounts for survey window effects."

As shown in Figure 2(a), we identify  $P = 152.39$  d as a significant period from the 1-term periodogram and 152.49 d from the 2-term periodogram. The 2-term periodogram also has large power at 304.81 d. Indeed, the 1-term and 2-term periodograms have significantly different values of power near  $\sim 300$  d, which is a harmonic of the  $\sim 150$  d

**Table 1.** The significant periods (in d) that we identified in each LS periodogram. We compute the means and standard deviations of single-wave periods and the double-wave. We also include the lines wavelengths from NIST's Atomic Spectra Database (Wiese 2000).

Spectral Line	LS Period	
	1-term	2-term
<b>Single-wave</b>		
$\text{He II } \lambda 4685.568$	$152.39 \pm 0.22$	$152.49 \pm 0.12$
$\text{He I } \lambda 5875.621$	$153.79 \pm 0.27$	$153.54 \pm 0.12$
$\text{H}\alpha \lambda 6562.819$	$153.06 \pm 0.28$	$153.15 \pm 0.15$
$\text{H}\beta \lambda 4861.350$	$154.25 \pm 0.28$	$153.49 \pm 0.11$
Mean $\pm$ Std Dev	$153.37 \pm 0.71$	$153.17 \pm 0.42$
<b>Double-wave</b>		
$\text{He II } \lambda 4685.568$	-	$304.81 \pm 0.44$
$\text{He I } \lambda 5875.621$	-	$307.35 \pm 0.49$
$\text{H}\alpha \lambda 6562.819$	-	$306.17 \pm 0.54$
$\text{H}\beta \lambda 4861.350$	-	$307.92 \pm 0.48$
Mean $\pm$ Std Dev	-	$306.56 \pm 1.19$

period. This difference is primarily due to the model and the way magnetospheric spectral lines can vary. The 1-term periodogram evaluates the least-squares fit for a single-wave sinusoidal model, while the 2-term fit can produce a double-wave model for the same period. The 1-term and 2-term periodograms both assign high power to the single-wave period around  $\sim 150$  d. For double-wave periods, the 1-term LS attempts to fit a single wave that spans  $\sim 300$  days, while the 2-term LS fits combinations of  $\sim 300$  d and  $\sim 150$  d waves (which better reproduce double high state cycles). Thus, the 2-term LS results in higher power around double wave periods than the 1-term.

For the uncertainty of the LS-derived periods, we use the analytic approximation provided by Horne & Baliunas (1986). All of the single-wave and double-wave periods with high LS power are listed in Table 1.

## 5. RESULTS

In this section, we discuss i) the periods that produce single-wave variations (one emission maximum per cycle) and ii) the periods that produce double-wave variations (two emission maxima per cycle and approximately twice as long as the single-wave). Subsequently, we assess the manner in which the EW time series phases according to these periods and investigate the periods' consistency with the ORM.

### 5.1. Periods yielding 'single-wave' variations

Figure 2(b) visually compares the periods reported in Table 1 to those from W12. Our objective is to determine a period that is overall compatible with the variations of all the spectral lines.

For the single-wave periods, the LS periodograms of each spectral line have significant peaks between 152.39 and

154.25 days, which are a few days shorter than the 157.99 d period of [W12](#). When comparing the values for each individual spectral line, it is apparent that all of our periods disagree with the values of [W12](#) for a given spectral line.

For our 1-term LS periods,  $\text{He II } \lambda 4686$  and  $\text{H}\beta$  agree at the  $4\sigma$  level, while other pairings agree within 2 to  $3\sigma$ . For the 2-term LS periods,  $\text{He II } \lambda 4686$  has a  $5\sigma$  agreement with  $\text{H}\beta$  and  $\text{He I } \lambda 5876$  while other pairings agree within 1 to  $3\sigma$ . For each spectral line, 1-term and 2-term counterparts agree at the 1 to  $2\sigma$  level.

We assess how effectively the periods phase the EW time series<sup>4</sup> and determine which ones produce the most coherent folded patterns. Figure 3 shows the collective phasing of each time series by a given period. We compare the 157.99 d period (upper row of panels) with the 2-term LS periods.

When we apply the [W12](#) period, all the phase-folded time series are disordered: the EWs of the newer observations (red and orange points) are significantly out of phase with the earliest ones (gray-scaled points). This is most apparent for the  $\text{He I } \lambda 5876$  and  $\text{He II } \lambda 4686$  EWs.

Applying the LS periods to their respective time series (i.e., the main diagonal of the bottom 4 rows) results in more coherent variability. For these periods, the measurements conform to a single-wave sinusoidal pattern, with maximum emission near  $\phi = 0.0$  and minimum emission near  $\phi = 0.5$ . The early epochs (black to gray) align more closely with the later ones (red to yellow).

We also examine how each of these four LS periods phases the EW of the other spectral lines (e.g., how well does the period derived from  $\text{H}\beta$  phase the EWs of  $\text{H}\alpha$ ,  $\text{He I } \lambda 5876$ , and  $\text{He II } \lambda 4686$ ). Comparing the largest period ( $P = 153.54$  d) with the other periods reveals that the EW measurements converge toward more coherent sinusoidal patterns as the period decreases. The 153.15 d and 152.49 d periods yield the most compact groupings between early- and late-epoch observations.

Additionally, there is notable scatter that none of the adopted periods could effectively remove. The measurements from rotations 10 to 15 (red) appear more coherent with  $P = 153.17$  d, whereas measurements from rotations 20 to 25 (orange) appear more coherent with  $P = 152.49$  d.

This behavior may be the consequence of cycle-to-cycle fluctuations in the magnetospheric emission. [ud-Doula et al. \(2013\)](#) produced 3D MHD simulations of a stellar magnetosphere similar to the magnetic O-type star  $\theta^1$  Ori C. They quantified the cycle-to-cycle scatter in observed and synthetic  $\text{H}\alpha$  EWs, and found that both had a standard deviation of  $\sim 0.25$  Å about a harmonic fit. With EWs variations from

-1 Å to 2 Å over rotational phase, this standard deviation corresponds  $\sim 0.1$  in normalized units.

We adopt the same approach to quantify the cycle-to-cycle scatter in our EWs, over our optimal range of periods. We fit a harmonic functions (same form as Eq. 2) with  $N = 2, 3, 4$ , find the coefficients with least-squares fitting, and compute the standard deviations of the residuals. Considering all of the lines together, the residual scatter is  $\sim 0.15$ . This value is much larger than the mean uncertainty of the normalized EWs ( $\sim 0.02$  level), but is comparable to [ud-Doula et al. \(2013\)](#). Increasing the number of harmonics does not significantly reduce the scatter, and the standard deviation remains nearly constant across our adopted period uncertainty.

Overall, a period 4 to 6 days shorter than that of [W12](#) produces more coherent, sinusoidal, modulated variations in the equivalent width measurements. Accordingly, for the remainder of our analysis, we adopt the mean and standard deviation of the 2-term LS periods,  $P = 153.17$  d  $\pm 0.42$  d (see the 153.15 d period shown in Figure 3 for a comparable reference).

In Figure 4(a), we directly examine the variations of the  $\text{He I}$  profiles as a function of phase using the adopted 153.17 d period. This approach allows us to identify any significant cycle-to-cycle discrepancies that are not apparent in the equivalent widths. The leftmost panel, which contains early-epoch observations, resembles that of Figure 1. This is expected, as this period is only slightly shorter than 157.99 d, and not enough time has elapsed (since  $\text{HJD}_0$ ) for significant phase drifting.

The second panel shows late-epoch observations. We find that the phasing of the profiles is consistent with early rotation cycles. Most notably, the  $\text{He I}$  profiles with complex morphologies appear to be confined to a phase interval of 0.3 to 0.7 for each epoch. Some discrepancies persist, such as near  $\phi \sim 0.7$ . We find that these discrepancies do not outweigh the overall improvements from using this period. The uncertainty in phase ( $\delta\phi$ ) increases as the time displacement relative to  $\text{HJD}_0$  does. For the observations in the second panel of Figure 4(a),  $\delta\phi \sim 0.03$  for some of the earliest observations (at  $N_{\text{rot}} = 10$ ), and  $\delta\phi \sim 0.07$  for the latest observation (at  $N_{\text{rot}} = 25$ ). Overall, from our set of single-wave periods, 153.17 d offers an optimal characterization of the variability of magnetospheric lines for NGC 1624-2.

### 5.1.1. The variation of $\langle B_z \rangle$ with a "single-wave" period

Next, we confirm whether the 153.17 d period is compatible with the variability of the magnetic field measurements. We apply this revised ephemeris to the independent sets of  $\langle B_z \rangle$  measurements reported by [DU2021](#) and [J2021](#). These measurements were made with the same ESPaDONs and NARVAL observations that we included in our spectroscopic

<sup>4</sup> We use the same  $\text{HJD}_0$  as [W12](#) in Equation 1.

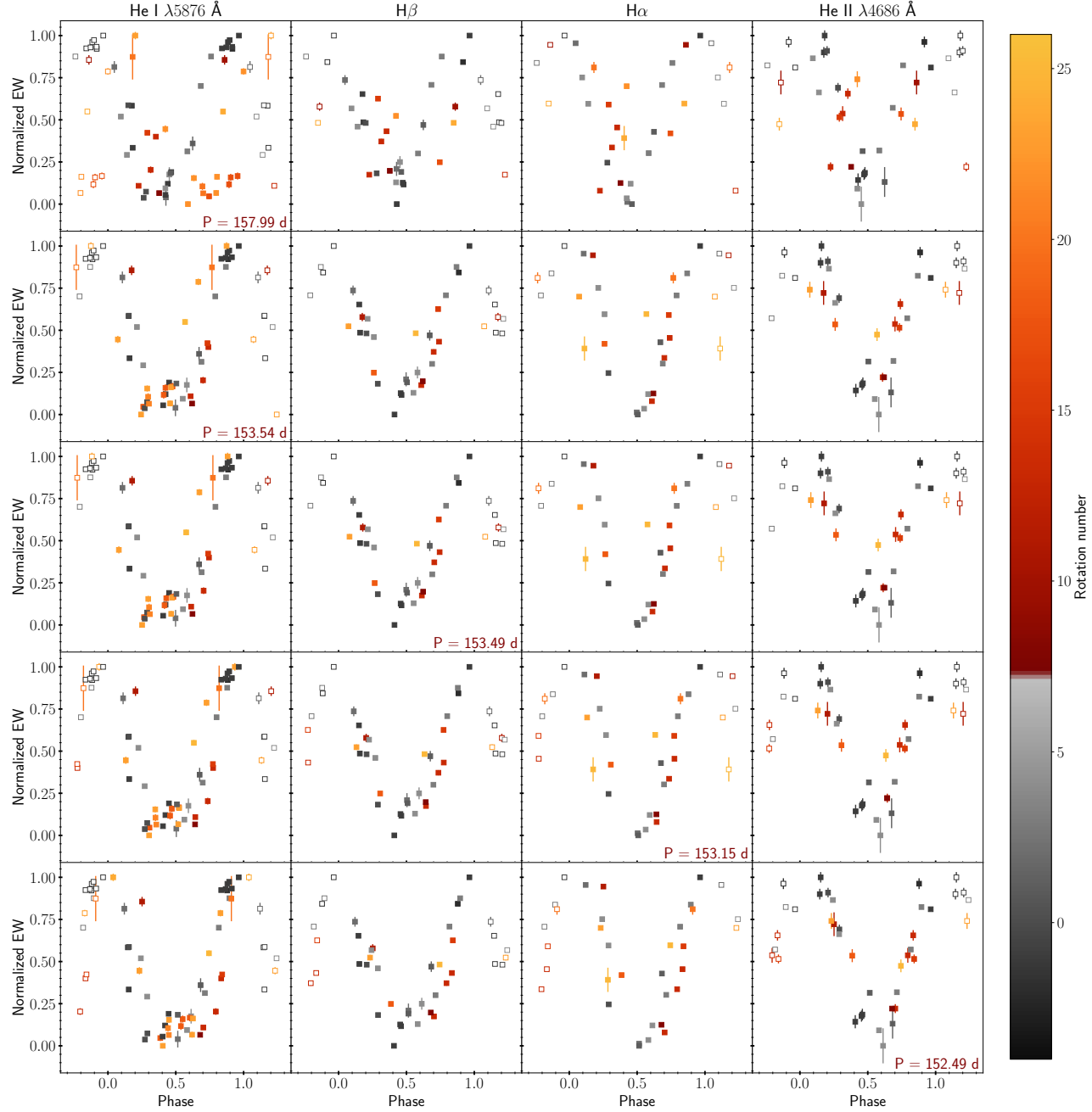


**Figure 3.** The variability of each EW time series using different periods. In the upper panels, the time series are phase-folded according to the W12 rotational period. In descending order of row, the four time series are phased by 153.54 d, 153.49 d, 153.15 d, and 152.49 d, which are all 2-term LS periods. The time series are vertically flipped and normalized so that 1 represents the most negative EWs (i.e. strongest emission/high state) and 0 indicates the opposite (i.e. weakest emission/ low state; recall that the low state He I profiles are complex). The measurements are colored according to their rotation numbers. To visually highlight the variation, we add unfilled duplicates of the first and last quarters of the time series.

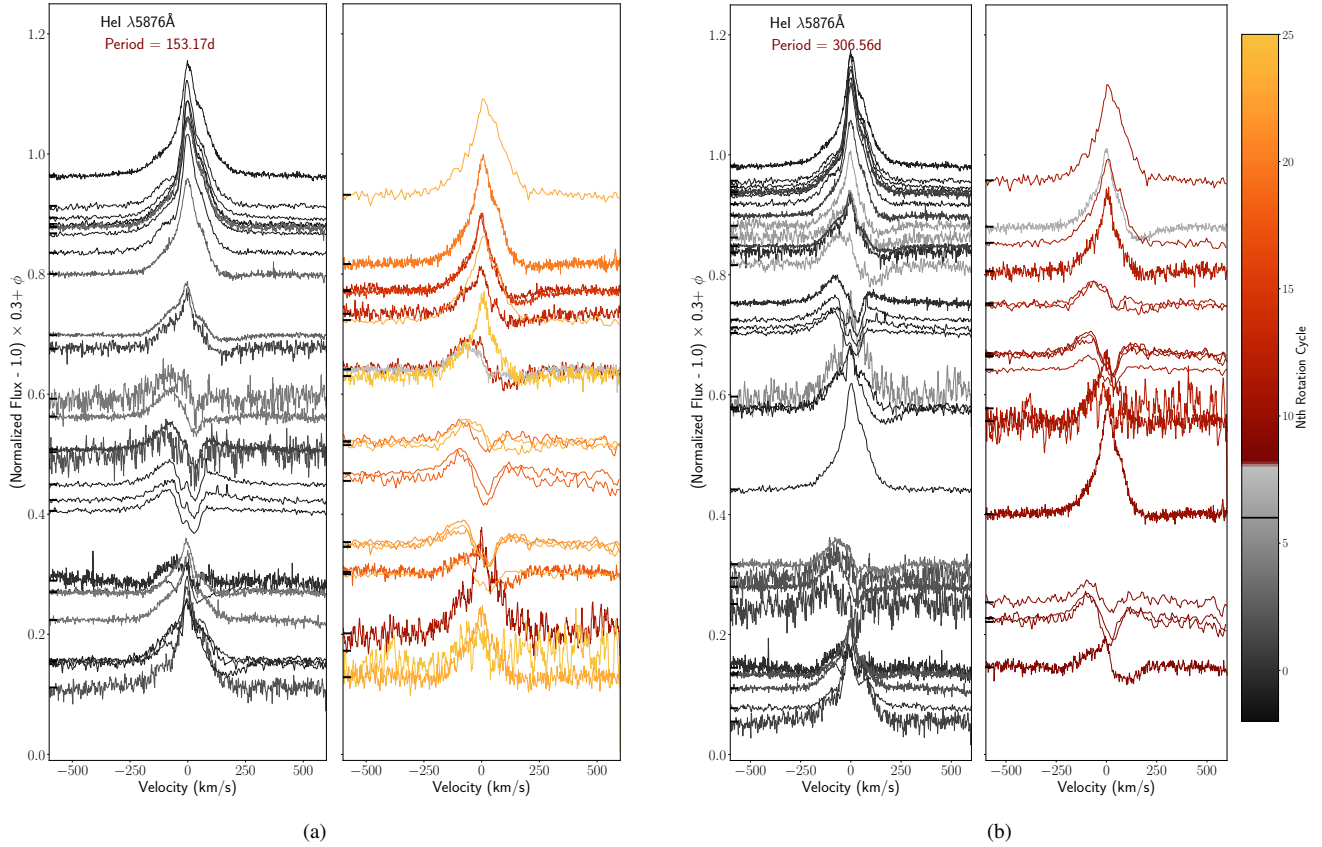


**Figure 4.** a) Same as Figure 1, but the panels use  $P = 153.17$  d to phase the profiles. b) Same as Figure 1, but the panels use  $P = 306.56$  d. Both figures share the same color, and the profiles are divided into the panels by  $N_{\text{rot}} < 6$ .

analysis<sup>5</sup>. In Figure 5(a), we compare the EW variations of all the spectral lines (top panels) and the  $\langle B_z \rangle$  measurements (bottom panels). We include sinusoidal fits to the  $\langle B_z \rangle$  data; the fit parameters, the amplitude, mean (vertical offset), and phase offset, are listed in Table B1.

The left panels of Figure 5(a) show the measurements phased with the 157.99 day period, and the middle panels show them phased with the  $P = 153.17$  d period. The right panel shows phasing with  $P = 306.56$  d, which we will discuss in Section 5.2.1.

Using the 153.17 d period instead of 157.99 d yields only minor changes to the phases and sinusoidal fits to the  $\langle B_z \rangle$  data. The magnetic measurements do not undergo large phase shifts from changing periods, as they are mostly from early-epoch observations. The  $\langle B_z \rangle$  fits maxima remain near 6 kG (4 kG for J2021) while the minima remain near 0 kG or very weakly negative. Overall, with the 153.17 day period, we find no contradiction between the variations of spectral lines and magnetic field measurements with respect to the ORM.

In summary, the single-wave periods that we obtain are all shorter than the 157.99 d period. When applied to equivalent widths, these shorter periods reduce the phase offsets that were observed in recent observations while using the 157.99 d period. We adopt the mean 2-term LS period of 153.17 d, which minimizes phase drifts of all spectral lines; although cycle-to-cycle variability persists. This shorter period also remains compatible with the magnetic datasets of DU2021 and J2021.

## 5.2. Periods yielding "double-wave" variations

We now consider the possibility of a period roughly twice that found in the previous section. As mentioned in Section 1, if the star has, e.g., a highly oblique dipolar field, then both poles can be significantly visible during a rotation cycle, and we would observe two high states over the course of one rotation.

The upper panel of Figure 2(b) presents a visual comparison of the significant double-wave periods. The periods derived from He II  $\lambda 4686$  and H $\beta$  agree at the  $4\sigma$  level, while remaining pairings agree within  $2\sigma$ . Overall, these periods are  $\sim 6$  to  $\sim 12$  d shorter than twice the W12 period ( $315.98 \pm 1.88$  d). We adopt the mean and standard deviation of the double-wave periods,  $P = 306.56$  d  $\pm 1.19$  d.

We do not replicate Figure 3 for the double-wave periods, as the phasing of the EW time series is similar for these periods. Using either the shortest (304.81 d) or longest (307.92 d) double-wave period instead of 306.56 d yields a maximum

phase shift of 0.06 on the last observation, which represents the largest possible phase offset. We therefore use the upper right panel of Figure 5(a) to show the impact of using a 306.56 d period on the EW variations. This 306.56 d period meets our expectations for double-wave variations of magnetospheric spectral lines. Two emission maxima (high states) occur within one cycle at  $\phi \sim 0.0$  and  $\phi \sim 0.5$ . There are also two emission minima (low states) at  $\phi \sim 0.25$  and  $\phi \sim 0.75$ . Although the two high-states appear to have similar amplitudes, the sampling of the mid-cycle high state is not sufficient to definitively determine this. We measure the cycle-to-cycle scatter in the same way as for the single-wave periods, and we get very similar results: there is constant residual scatter at the 0.15 level, in the range of period around our nominal double-wave period.

As was done in Section 5.1, we examine the variation of HeI profiles when phase-folded with the 306.56 d period, as shown by Figure 4(b). In both panels, the complex HeI profiles are grouped around  $\phi \sim 0.25$  and  $\phi \sim 0.75$ . Strong emission profiles occur at the start of the cycle ( $\phi \sim 0.0$ ) as well as at  $\phi \sim 0.5$ . The smooth transitions between strong emission and complex morphologies are consistent with the high states and low states observed in the EW variation in Figure 5(a). Some phasing discrepancies remain, such as at  $\phi \sim 0.8$ . However, for the observation in the right panel of Figure 4(b),  $\delta\phi \sim 0.02$  at  $N_{\text{rot}} = 6$  and  $\delta\phi \sim 0.05$  for the most recent observation ( $N_{\text{rot}} = 12$ ). Overall, the variability of the spectral lines appear compatible with a 306.56 d double-wave period.

### 5.2.1. The variation of $\langle B_z \rangle$ with a "double-wave" period

We examine the co-variations of the EW and  $\langle B_z \rangle$  measurements when phased with the 306.56 d period. In Figure 5(a) (lower right panel), the  $\langle B_z \rangle$  measurements from both studies are well fitted by the sinusoidal curves. The quality of the  $\langle B_z \rangle$  fits improves significantly when adopting the longer period (see reduced  $\chi^2$  values listed in Table B1). We find that the variations of the  $\langle B_z \rangle$  measurements (and their sinusoidal models) are consistent with the EW datasets, with extrema of  $\langle B_z \rangle$  occurring at the same phase as the EW emission maxima, as expected. At the start of the cycle ( $\phi \sim 0.0$ ), the mean longitudinal field reaches its strongest positive value; it is  $\langle B_z \rangle \sim 5.11$  kG and 3.30 kG for the DU2021 and J2021 datasets, respectively. The near-zero  $\langle B_z \rangle$  measurements are instead distributed between two separate EW low states at  $\phi \sim 0.25$  and  $\sim 0.75$ .

The sinusoidal models also predict the magnetic South pole approaching the line of sight, yielding strongly negative minima (of  $-4.19$  kG for the DU2021 measurements and  $-2.74$  kG for J2021) that coincide with an EW high state at  $\phi \sim 0.5$ . Overall, the variability of the EW and  $\langle B_z \rangle$  measurements is

<sup>5</sup> We note that J2021 has a larger set of measurements than DU2021 as they did not co-add the ESPaDOnS observations taken during the same night. We opted to use the measurements from J2021 that included all applicable lines in the Least-Squares Deconvolution profiles

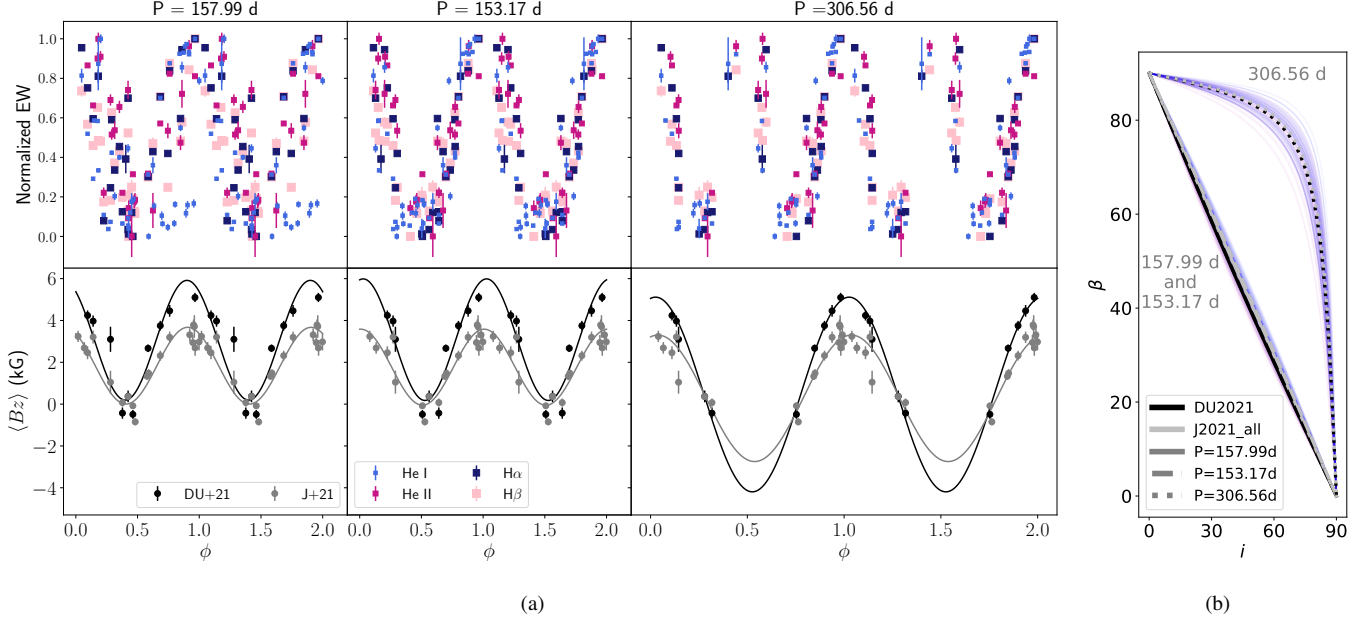


**Figure 5.** a) The variability of the normalized EW time series (He I, He II, H $\alpha$ , and H $\beta$ ; top panels) and the  $\langle B_z \rangle$  measurements from DU2021 and J2021 (bottom panels) using the 157.99 d, 153.17 d, and 306.56 d periods. The data are replicated over two rotation cycles for visual enhancement. b) Relationship between  $i$  and  $\beta$  that is implied by the min-to-max ratio of the best fitting sinusoid curves to the  $\langle B_z \rangle$  measurements. The three types of dashed curves show the  $i - \beta$  curves derived for the DU2021 (black) and J2021 (gray) datasets using each period. The colored curves are the  $i - \beta$  curves resulting from samples drawn from the MCMC fit posterior distribution; the pink and purple curves are from fits to DU2021 and J2021, respectively; the set of lower curves is from using the single-wave periods, and the set of higher curves is from the double-wave period.

consistent with  $P = 306.56$  d within the framework of the ORM and magnetospheric emission.

Importantly, no existing spectropolarimetric observations are within the phase interval during which the double-wave models predict strongly negative  $\langle B_z \rangle$  measurements. Consequently, the existing longitudinal field dataset is unable to distinguish between the single-wave and double-wave solutions.

## 6. DISCUSSION AND CONCLUSIONS

We analyzed the variability of magnetospheric spectral lines of NGC 1624-2 in order to update the measurement of the rotation period. We used the LS method on EW measurements of spectral lines from both new and archival observations. Additionally, we assessed how well the identified periods phased the EWs, the line profiles, and the literature  $\langle B_z \rangle$  measurements (from DU2021 and J2021). From the periodograms, we found periods that phase the EW time series into single-wave and double-wave variations. We adopted  $153.17 \pm 0.42$  d as the single-wave period and  $306.52 \pm 1.19$  d as the double-wave period.

Both periods are effective in reducing the late-epoch phase drifts that were present whenever the 157.99 d period (W12) was used. The single-wave or double-wave periods produce coherent variations in the EW and line profile time series.

We found that some scatter remained present in the phased equivalent width measurements, regardless of which period we used. This is not entirely surprising, as cycle-to-cycle fluctuations are observed in other magnetic O stars (HD 148937, Of?p; Wade et al. 2012b and  $\theta^1$  Ori C, O7f?p; Stahl et al. 2008; Maíz Apellániz et al. 2019b). The investigation by ud-Doula et al. (2013) into the stochasticity of magnetospheric H $\alpha$  emission from  $\theta^1$  Ori C found that over-densities of infalling material were the main sources of the fluctuations and contributed to the azimuthal fragmentation of breakout outflows above the Alfvén radius. Our measurement of the scatter in our EWs is at the same level as that reported by ud-Doula et al. (2013), and they do not differ significantly between single and double-wave periods. Because the harmonic fits return similar residuals, this suggests that i) cycle-to-cycle variations are present, and ii) the variation of the EWs cannot distinguish between the single-wave and double-wave periods.

### 6.1. Magnetic Geometry

The variations of the  $\langle B_z \rangle$  measurements reported by DU2021 and J2021 are compatible with both rotational periods, thus confirming consistency with the ORM. However, the double-wave period reveals a sizable gap in spectropolarimetric coverage, which leaves us unable to definitively determine which period is correct. This gap is likely a dual-consequence

of the visibility window from CFHT and the timing of observations. If the star actually completes its rotations in just under a year and the north pole was in view at discovery, the south pole would not have been visible from CFHT for a few years post-discovery.

The two possible rotational periods correspond to very different magnetic configurations.

The **single-wave period** corresponds to a configuration in which only the North magnetic pole comes into view during a stellar rotation. As shown in Figure 5(a), our single-wave period does not significantly impact the phasing of the spectropolarimetric measurements, as they were all taken at an early epoch. Thus, our result for the single-wave variations unsurprisingly matches the configuration inferred by W12 (and revisited by DU2021 and J2021).

We provide Figure 5(b) to show the constraints between  $i$  and  $\beta$  implied by the sinusoidal fits to the  $\langle B_z \rangle$  data in Figure 5(a), as described by Preston (1967). We derive the Preston  $r$ -value which is the ratio of  $\langle B_z \rangle$  extrema ( $r = B_{min}/B_{max}$ ). After calculating  $r$ , we evaluate  $i$  with respect to  $\beta$  using  $\tan(i) = ((1 - r)/(1 + r)) \cot(\beta)$ . Each curve represents a Markov Chain Monte Carlo (MCMC) sample in the posterior probability. Broadly, the fits have a Preston  $r$ -value close to zero, and the magnetic configuration is such that  $i + \beta$  is roughly 90 degrees.

The **double-wave period** corresponds to a configuration in which both poles are visible. As shown in Figure 5(a), adopting this period significantly alters the phases of spectropolarimetric measurements. Our model reproduces the measurements well and reaffirms the observation of the northern magnetic hemisphere. However, due to the gap in coverage, we also interpret the EW curves. For double-wave variation, the high state peaks of the EWs can differ in amplitude depending on the relative tilt of the two magnetic poles when each is closest to the line of sight. When using the double-wave period for NGC 1624-2, we do not observe any clear asymmetries between the EW high states. That said, the mid-cycle high state is not fully covered, even with our new spectroscopic observations. At present, the high state appears to have an amplitude at least comparable to the one coinciding with the North magnetic pole. This suggests that the  $\langle B_z \rangle$  variation is more symmetric about zero, implying a magnetic field that may be more tilted than originally inferred.

Our fit of the  $\langle B_z \rangle$  data phased with the double-wave period supports a large obliquity or inclination angle. As seen in Figure 5(a), the  $\langle B_z \rangle$  fit predicts extrema of similar strengths, with a Preston  $r$ -value close to -1. Figure 5(b) shows the resulting constraints on  $i$  and  $\beta$  for this period. Broadly, either  $\beta$  has to be close to 90 degrees (for any non-zero values of  $i$ ) or  $i$  has to be close to 90 degrees (for any non-zero values of  $\beta$ ). Within these constraints, smaller values of  $i$  or  $\beta$  require a stronger dipolar field to reproduce the  $\langle B_z \rangle$  extrema.

For a 306 d period, an estimated stellar radius of  $10R_{\odot}$  yields an equatorial rotational velocity of  $\sim 1.5$  km/s, consistent with the inferred  $v \sin i < 3$  km/s. However, this offers no meaningful constraint on the inclination angle.

At present, we are unable to distinguish between the single- and double-wave periods with only EWs. Given the available data and the level of cycle-to-cycle variability, it is unlikely that spectroscopy alone can resolve this ambiguity, especially if the magnetic geometry results in emission maxima of similar amplitude. The most straightforward approach to discern between the single- and double-wave periods is to obtain at least one Stokes  $V$  observation within the phase interval where the double-wave period predicts that the (yet unobserved) South pole would come into view.

## 6.2. Revisiting Phasing in Previous Studies

We now address the implications of the two rotation periods on previous magnetospheric studies of NGC 1624-2. We specifically revisit the UV observations reported by DU2021, and the X-ray analysis of Petit et al. (2015).

### 6.2.1. UV Observations

David-Uraz et al. (2019, 2021) observed the UV resonance spectral lines formed in the winds of O stars. As wind lines are usually very sensitive to the density and kinematics of the stellar outflows, the break in spherical symmetry caused by the magnetosphere is expected to have a significant impact on the shape of the line profiles (Sundqvist et al. 2014; Erba et al. 2021). They found that the variations of the CIV  $\lambda\lambda 1548, 1550$  Å and SiIV  $\lambda\lambda 1393, 1402$  Å doublets were quite extreme, and that their shapes were not compatible with spherically symmetric winds. In light of our revised periods, we revisit their findings in which the variation of the line profiles as a function of phase was not what one would expect from the magnetic geometry assumed at the time.

In Figure 6 (left panel), we reproduce Figure 1 of DU2021. In this figure, the initial observations by David-Uraz et al. (2019) (bold) served as a reference to categorize the follow-up spectra by their morphology. Blue and red indicate observations that have similar line morphologies as the reference high state and low state observations, respectively. DU2021 focused on CIV and SiIV doublets, given their value as magnetospheric probes (we refer to DU2021 and Nazé et al. 2015 for details).

With a single-wave period, DU2021 expected the line profile morphology to transition from a high state near phase 0 to a low state at phase 0.5 and back to a high state at phase 1.0. However, as seen in the leftmost panels of the figure, they found that the 157.99 d period does not phase the UV observations in a continuous single-wave variation.

In the middle panel of Figure 6, we apply our single-wave ephemeris to phase the UV data. There is now a consistent,

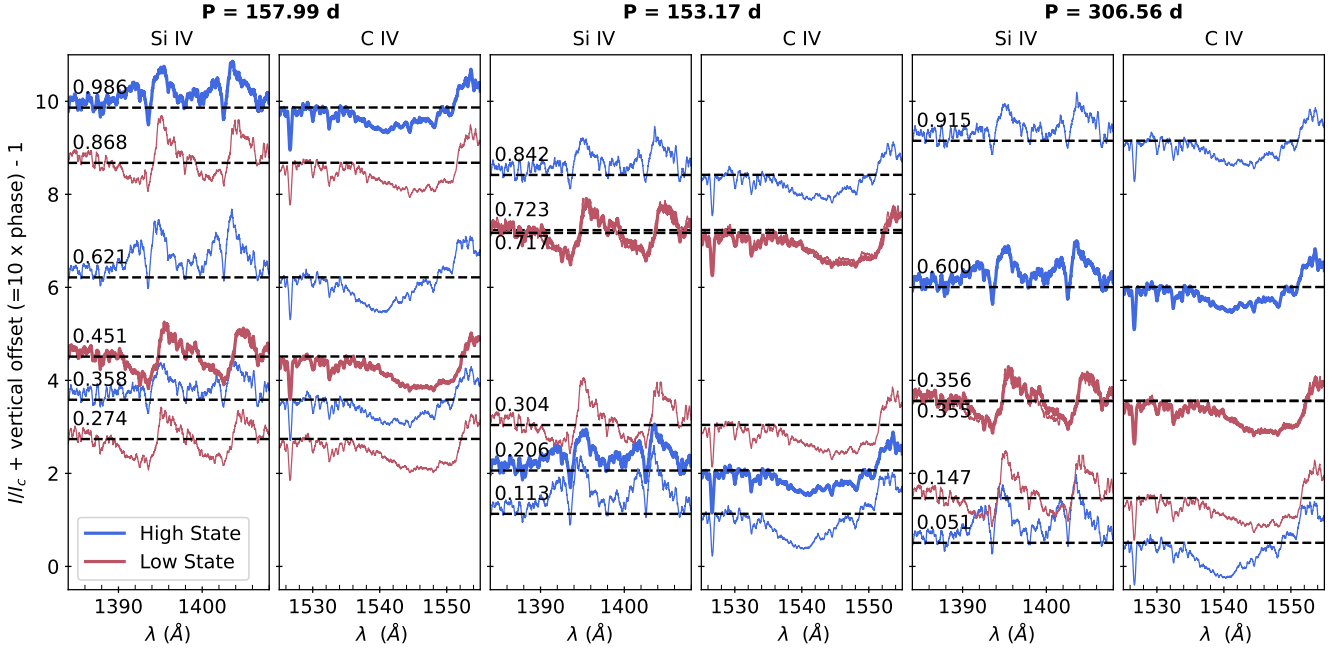


**Figure 6.** Profiles of the CIV and SiIV wind-sensitive resonance lines for NGC 1624-2 that were studied by DU2021. In the same manner as Figure 1, the profiles are arranged vertically according to phase (scaled up by a factor of 10 as in DU2021). The observations with thicker lines are the earlier-epoch high state (blue) and low state (red) that were reported in David-Uraz et al. (2019). The others are follow-up observations with the color assigned by DU2021 according to which of the two reference observations they resembled the most. In the middle and right panels, we phase the observations according to our single-wave and double-wave ephemerides.

smooth transition from high state-like to low state-like morphologies. The shift in phasing of the UV observations is large because they were obtained at late epochs with respect to HJD<sub>0</sub> (rotations 14 and 16) and have accumulated a larger phase difference than, e.g. the archival spectropolarimetric observations. In other words, these observations were not obtained at their intended rotational phases.

The right panel of Figure 6 shows the UV observations phased with the 306.56 d period. As expected, we see a double-wave variation of the spectral lines. With this period, two of the observations would correspond to the North high state, and one to the South high state. Two observations would correspond to nearly the same rotational phase ( $\sim 0.35$ ), and the agreement between the two observations is very good.

#### 6.2.2. X-ray Observations

Petit et al. (2015) conducted a follow-up X-ray analysis to W12 with two Chandra observations targeting the high state and low state, as predicted with the W12 ephemeris. They found variable emission that could only be modeled with a strong source of soft X-rays that is heavily attenuated at low energies. This finding is consistent with a model in which X-rays are generated by magnetically confined wind shocks (Babel & Montmerle 1997; ud-Doula et al. 2014) and are partially reabsorbed by the extensive, cooled magnetospheric material.

We confirm that these observations captured their intended magnetospheric states when adopting either of our derived rotation periods. These observations were acquired within a maximum of 4 rotations from the zero-date of the ephemeris, so the accumulated phase offsets are minimal. The low state observation's (HJD 2456508.20) phase changes from 0.43 to 0.53 with our 153.17 d period and to 0.77 with the 306.56 d period (which is the low state following the visibility of the negative magnetic pole). The high state observation's (HJD 2456592.84) phase changes from 0.96 to 0.09 with the 153.17 d period and to 0.04 with the 306.56 d period (which would be a North high state observation).

#### 6.3. Conclusion

We have identified two periods that can simultaneously phase the magnetospheric and magnetic measurements of NGC 1624-2 and reopened questions regarding the star's magnetic field configuration.

Our analysis of magnetospheric spectral line time series has led us to a single-wave period of 153.17 d, which is only a few days shorter than the current rotation period on record. Using the currently accepted 157.99 d period would result today in an accumulated phase error of  $\sim 0.16$ . Our shorter period still represents the originally inferred geometry that brings only one pole into view over the course of the rotation. This new single-wave period can reliably be used to schedule

observations for studies that do not rely on the polarity of the high state.

We also find that 306.56 days, which implies a geometry that allows both poles to be visible, is an equally suitable period. A spectropolarimetric observation obtained at the expected South pole high state would straightforwardly distinguish between a single-wave or a double-wave magnetic configuration.

#### STATEMENT OF DATA AVAILABILITY

The observations are available as follows: *HST* COS data are archived under MAST: [10.17909/d8mf-2v58](https://doi.org/10.17909/d8mf-2v58), ESPaDOnS and DAO via the Canadian Astronomical Data Centre, Narval via [Polarbase](#)(Petit et al. 2014), and the remaining data in their respective project repositories (or requested from the survey first authors). The optical observations and analysis are available in ZENODO via <https://doi.org/10.5281/zenodo.1795304>.

#### ACKNOWLEDGEMENTS

SS acknowledges support for this work from the Delaware Space Grant College and Fellowship Program (NASA Grant 80NSSC20M0045).

This material is based upon work supported by the National Science Foundation under Grant No. AST-2108455 (SS, VP, JM). MEO gratefully acknowledges support for this work from the National Science Foundation under Grant No. AST-2107871.

The authors would like to extend our thanks to the anonymous referees who provided numerous helpful comments that improved this paper.

This work was made possible by observations obtained with the Canada–France–Hawaii Telescope (CFHT), which is operated by the National Research Council (NRC) of Canada, the Institut National des Sciences de l’Univers of the Centre National de la Recherche Scientifique (CNRS) of France, and

the University of Hawaii. This work was made possible by observations obtained with the Narval spectropolarimeter at the Telescope Bernard Lyot, Observatoire du Pic du Midi, CNRS/INSU, and Université de Toulouse, France. This work was made possible by observations obtained with the HERMES spectrograph, which is supported by the Research Foundation - Flanders (FWO), Belgium, the Research Council of KU Leuven, Belgium, the Fonds National de la Recherche Scientifique (F.R.S.-FNRS), Belgium, the Royal Observatory of Belgium, the Observatoire de Genève, Switzerland, and the Thüringer Landessternwarte Tautenburg, Germany. This work was made possible by observations collected in the IACOB spectroscopic database maintained by the Nordic Optical Telescope Scientific Association using the Nordic Optical Telescope. This work was made possible by observations collected with the Mercator Telescope on the island of La Palma at the Spanish Observatorio del Roque de los Muchachos of the Instituto de Astrofísica de Canarias. This work was made possible by observations obtained by the Dominion Astrophysical Observatory, which is part of the Herzberg Astronomy and Astrophysics Research Centre, under the National Research Council of Canada. This work was made possible by observations obtained by the Hobby-Eberly Telescope (HET) at the Texas McDonald Observatory, a joint project of the University of Texas at Austin, the Pennsylvania State University, Ludwig-Maximilians-Universität München, and Georg-August-Universität Göttingen. This work was made possible by observations collected at the Calar Alto Observatory. This work was made possible by observations made with the NASA/ESA Hubble Space Telescope obtained from the Space Telescope Science Institute, which is operated by the Association of Universities for Research in Astronomy, Inc., under NASA contract NAS 5-26555. These observations are associated with program HST-GO-15066.001-A. This research has made use of data obtained from the Chandra Data Archive and the Chandra Source Catalog, both provided by the Chandra X-ray Center (CXC).

#### APPENDIX

##### A. THE LOG OF OBSERVATIONS

Table A1 provides a log of all observations used. We estimate the SNR’s using a portion of the continuum on the red side of each spectral line. We include the equivalent widths that comprise each time series. We exclude a MERCATOR (2022-08-31) observation from the calculation of any spectral time series due to high noise. We omit two CAFE BEANS ( 2012-12-28 and 2013-02-26) observations from the He II  $\lambda 4686$  time series and one (2020-11-02) from both the He II  $\lambda 4686$  and H $\beta$  time series due to significant noise. Due to evidence of saturation, we omit all NoMaDs observations from the H $\alpha$  time series.

**Table A1.** The log of observations used in this work. We list the date, instrument, and exposure time, SNR's and EW measurements from each observation. We use shortened labels indicate the instruments: ESPaDOnS (ESP), NARVAL (NAR), NoMaDs(NOM), HERMES (MER), FIES (IAC), CAFÉ-BEANS (CAF). Observations acquired by the same instrument on the same night (or within one day of each other) are coadded, and we adopt the mean HJD for the spectral line time series. Some sets of ESPaDOnS observations are the exception: we coadd the observations acquired between 2012-02-01 and 2012-02-09 and those acquired between 2013-08-27 and 2013-08-29

Date	Obs.	HJD	Exp. (s)	Signal-to-Noise Ratios				Equivalent Width Measurements (km/s)							
				- 2450000.0	He I	He II	H $\alpha$	H $\beta$	He I	$\sigma$	He II	$\sigma$	H $\alpha$	$\sigma$	H $\beta$
2011-08-22	NOM (BGRV)	5795.963	650	101.0	117.0	77.0	60.0	-84.6	0.6	-63.0	1.3	-	-	-241.21	0.46
2011-10-02	NOM (BGRV)	5836.866	900	53.0	102.0	18.0	59.0	-54.6	0.9	-60.5	1.3	-	-	-220.73	0.54
2011-10-03	NOM (BGRV)	5837.860	900	74.0	147.0	91.0	57.0	-32.4	0.8	-64.5	1.2	-	-	-202.71	0.40
2011-11-10	NOM (RV)	5875.953	900	116.0	-	87.0	-	-7.6	0.5	-	-	-	-	-	-
2011-11-11	NOM (BG)	5876.716	1800	-	95.0	-	60.0	-	-	-30.3	1.6	-	-	-150.37	0.48
2011-11-13	NOM (RV)	5878.708	900	107.0	-	81.0	-	-13.4	0.6	-	-	-	-	-	-
2011-11-17	NOM (RV)	5882.707	900	118.0	-	68.0	-	-19.6	0.5	-	-	-	-	-	-
2011-11-18	NOM (BG)	5883.697	1800	-	114.0	-	63.0	-	-	-31.7	1.3	-	-	-164.01	0.44
2011-11-19	NOM (BG)	5884.691	1800	-	113.0	-	64.0	-	-	-32.0	1.4	-	-	-162.91	0.44
2012-01-15	NOM (VR)	5941.783	900	122.0	-	84.0	-	-84.9	0.6	-	-	-	-	-	-
2012-01-20	NOM (VR)	5946.755	900	146.0	-	67.0	-	-85.4	0.5	-	-	-	-	-	-
2012-01-22	NOM (VR)	5948.749	900	110.0	-	50.0	-	-88.1	0.6	-	-	-	-	-	-
2012-01-24	NOM (VR)	5950.756	900	153.0	-	93.0	-	-89.2	0.5	-	-	-	-	-	-
2012-01-27	NOM (VR)	5953.743	900	100.0	-	47.0	-	-85.7	0.6	-	-	-	-	-	-
2012-02-01	ESP	5958.715	2400	138.0	141.0	93.0	59.0	-91.6	0.2	-56.9	0.3	-1236.3	0.4	-258.13	0.33
2012-02-02	ESP	5959.716	2400	-	-	-	-	-	-	-	-	-	-	-	-
2012-02-03	ESP	5960.713	2400	-	-	-	-	-	-	-	-	-	-	-	-
2012-02-04	ESP	5961.713	2400	-	-	-	-	-	-	-	-	-	-	-	-
2012-02-09	ESP	5966.720	2400	-	-	-	-	-	-	-	-	-	-	-	-
2012-03-04	NOM (VR)	5990.621	900	100.0	-	42.0	-	-54.9	0.6	-	-	-	-	-	-
2012-03-12	NOM (BG)	5998.600	1800	-	153.0	-	62.0	-	-	-60.9	1.1	-	-	-202.25	0.41
2012-03-22	NOM (VR)	6008.596	900	130.0	-	63.0	-	-6.1	0.6	-	-	-	-	-	-
2013-03-24	NAR	6011.332	4800	36.0	30.0	30.0	31.0	-9.3	0.7	-52.1	1.1	-888.8	1.1	-170.05	0.97
2012-09-27	ESP	6197.944	5400	142.0	114.0	82.0	60.0	-19.1	0.2	-37.2	0.3	-775.4	0.3	-170.95	0.30
2012-09-27	ESP	6198.009	5400	-	-	-	-	-	-	-	-	-	-	-	-
2012-10-23	CAF	6223.633	3600	36.0	22.0	41.0	19.0	-34.7	3.6	-29.9	3.5	-973.1	4.8	-201.01	3.36
2012-12-28	CAF	6290.400	3600	32.0	19.0	31.0	12.0	-75.0	3.1	-	-	-1215.4	4.1	-229.71	3.14
2013-02-26	CAF	6350.464	3600	20.0	8.0	18.0	8.0	-6.3	4.4	-	-	-781.2	5.8	-172.89	4.50
2013-08-27	ESP	6532.119	5160	167.0	115.0	94.0	53.0	-30.5	0.2	-37.3	0.2	-914.8	0.3	-182.75	0.26
2013-08-29	ESP	6534.056	5160	-	-	-	-	-	-	-	-	-	-	-	-
2013-08-29	ESP	6534.118	5160	-	-	-	-	-	-	-	-	-	-	-	-
2013-09-13	ESP	6549.033	5160	140.0	106.0	71.0	50.0	-65.0	0.2	-47.4	0.3	-1101.2	0.3	-226.62	0.31
2013-09-13	ESP	6549.096	5160	-	-	-	-	-	-	-	-	-	-	-	-
2013-09-25	ESP	6561.024	5160	115.0	93.0	66.0	52.0	-80.6	0.3	-57.4	0.3	-1161.6	0.4	-244.74	0.37
2013-09-25	ESP	6561.086	5160	-	-	-	-	-	-	-	-	-	-	-	-
2013-11-17	ESP	6613.909	5160	124.0	107.0	65.0	56.0	-48.9	0.3	-59.1	0.3	-1121.8	0.4	-211.57	0.37
2013-11-17	ESP	6614.041	5160	-	-	-	-	-	-	-	-	-	-	-	-
2013-11-24	ESP	6621.036	5160	121.0	87.0	73.0	53.0	-28.7	0.3	-51.0	0.3	-1049.8	0.4	-199.91	0.37
2013-11-24	ESP	6621.098	5160	-	-	-	-	-	-	-	-	-	-	-	-
2014-01-08	ESP	6665.822	5160	91.0	87.0	71.0	51.0	-11.1	0.3	-28.3	0.3	-791.4	0.4	-164.27	0.40

2014-01-08	ESP	6665.884	5160	-	-	-	-	-	-	-	-	-	-	-	-	-
2014-01-12	CAF	6670.413	3600	23.0	8.0	23.0	10.0	-18.3	3.9	-24.7	4.1	-831.2	5.0	-177.26	3.80	
2015-09-24	ESP	7290.036	5160	91.0	84.0	46.0	48.0	-8.5	0.3	-33.5	0.4	-833.0	0.4	-171.64	0.44	
2015-09-25	ESP	7291.054	5160	-	-	-	-	-	-	-	-	-	-	-	-	-
2016-10-21	MER	7682.744	1800	14.0	8.0	14.0	6.0	-78.8	2.5	-53.4	2.8	-1211.0	3.1	-212.69	2.65	
2017-10-30	MER	8056.556	3600	39.0	25.0	27.0	18.0	-12.4	0.9	-33.5	1.1	-812.0	1.2	-169.17	0.98	
2017-11-13	IAC	8070.611	3600	43.0	21.0	47.0	24.0	-20.8	1.8	-46.0	1.8	-930.3	2.3	-190.43	1.66	
2017-11-19	IAC	8076.660	5400	61.0	36.0	49.0	36.0	-38.3	1.2	-50.8	1.2	-985.0	1.6	-196.94	1.17	
2018-09-21	IAC	8382.717	3600	74.0	39.0	55.0	35.0	-40.4	1.0	-45.2	1.1	-1047.6	1.4	-217.81	1.01	
2019-10-14	IAC	8770.613	2400	47.0	25.0	37.0	26.0	-6.8	1.5	-45.9	1.5	-968.9	2.0	-177.16	1.46	
2019-11-06	dao	8793.798	1800	50.0	-	-	-	-13.1	2.0	-	-	-	-	-	-	
2019-11-06	dao	8793.819	1800	-	-	-	-	-	-	-	-	-	-	-	-	
2019-11-06	dao	8793.841	1800	-	-	-	-	-	-	-	-	-	-	-	-	
2019-11-06	dao	8793.862	1800	-	-	-	-	-	-	-	-	-	-	-	-	
2019-11-08	dao	8795.760	1800	115.0	-	-	-	-16.8	1.9	-	-	-	-	-	-	
2019-11-08	dao	8795.782	1800	-	-	-	-	-	-	-	-	-	-	-	-	
2019-11-08	dao	8795.803	1800	-	-	-	-	-	-	-	-	-	-	-	-	
2019-11-08	dao	8795.831	1800	-	-	-	-	-	-	-	-	-	-	-	-	
2019-11-16	dao	8803.778	1800	63.0	-	-	-	-17.5	1.8	-	-	-	-	-	-	
2019-11-16	dao	8803.799	1800	-	-	-	-	-	-	-	-	-	-	-	-	
2019-11-16	dao	8803.821	1800	-	-	-	-	-	-	-	-	-	-	-	-	
2020-11-02	CAF	9155.513	1800	-	-	-	-	-	-	-	-	-	-	-	-	
2021-01-22	dao	9236.758	1800	67.0	-	-	-	-12.1	1.9	-	-	-	-	-	-	
2021-01-22	dao	9236.789	1800	-	-	-	-	-	-	-	-	-	-	-	-	
2021-01-22	dao	9236.810	1800	-	-	-	-	-	-	-	-	-	-	-	-	
2021-01-22	dao	9236.831	1800	-	-	-	-	-	-	-	-	-	-	-	-	
2021-01-23	dao	9237.677	1800	106.0	-	-	-	-8.4	1.3	-	-	-	-	-	-	
2021-01-23	dao	9237.698	1800	-	-	-	-	-	-	-	-	-	-	-	-	
2021-01-23	dao	9237.719	1800	-	-	-	-	-	-	-	-	-	-	-	-	
2021-01-23	dao	9237.740	1800	-	-	-	-	-	-	-	-	-	-	-	-	
2021-01-23	dao	9237.771	1800	-	-	-	-	-	-	-	-	-	-	-	-	
2021-01-23	dao	9237.792	1800	-	-	-	-	-	-	-	-	-	-	-	-	
2021-10-22	IAC	9509.608	1037	30.0	23.0	26.0	22.0	-42.3	1.9	-54.2	1.9	-1097.9	2.5	-206.78	1.79	
2021-11-17	dao	9535.886	1800	112.0	-	-	-	-2.7	1.4	-	-	-	-	-	-	
2021-11-17	dao	9535.908	1800	-	-	-	-	-	-	-	-	-	-	-	-	
2021-11-17	dao	9535.929	1800	-	-	-	-	-	-	-	-	-	-	-	-	
2021-11-24	dao	9542.838	1800	99.0	-	-	-	-16.5	1.6	-	-	-	-	-	-	
2021-11-24	dao	9542.859	1800	-	-	-	-	-	-	-	-	-	-	-	-	
2021-12-20	dao	9568.771	1800	61.0	-	-	-	-8.6	1.5	-	-	-	-	-	-	
2021-12-20	dao	9568.792	1800	-	-	-	-	-	-	-	-	-	-	-	-	
2021-12-20	dao	9568.813	1800	-	-	-	-	-	-	-	-	-	-	-	-	
2021-12-20	dao	9568.834	1800	-	-	-	-	-	-	-	-	-	-	-	-	
2021-12-21	dao	9569.765	1800	105.0	-	-	-	-17.1	1.4	-	-	-	-	-	-	
2021-12-21	dao	9569.786	1800	-	-	-	-	-	-	-	-	-	-	-	-	
2021-12-21	dao	9569.807	1800	-	-	-	-	-	-	-	-	-	-	-	-	
2021-12-21	dao	9569.828	1800	-	-	-	-	-	-	-	-	-	-	-	-	
2022-01-21	dao	9600.683	1800	126.0	-	-	-	-72.7	1.7	-	-	-	-	-	-	
2022-01-21	dao	9600.704	1800	-	-	-	-	-	-	-	-	-	-	-	-	
2022-01-21	dao	9600.725	1800	-	-	-	-	-	-	-	-	-	-	-	-	
2022-02-22	dao	9632.629	1800	59.0	-	-	-	-91.6	2.0	-	-	-	-	-	-	

2022-02-22	dao	9632.650	1800	-	-	-	-	-	-	-	-	-	-	-	-	-
2022-02-22	dao	9632.671	1800	-	-	-	-	-	-	-	-	-	-	-	-	-
2022-02-22	dao	9632.691	1800	-	-	-	-	-	-	-	-	-	-	-	-	-
2022-08-31	MER	9822.680	1800	7.0	4.0	7.0	3.0	-	-	-	-	-	-955.9	33.2	-	-
2022-11-09	IAC	9892.758	1200	38.0	35.0	26.0	30.0	-51.5	1.5	-43.5	1.5	-1050.3	2.0	-202.34	1.43	

## B. SINUSOIDAL MODELS OF THE $\langle B_z \rangle$ TIME SERIES

For each  $\langle B_z \rangle$  dataset paired with each period, we use the Nelder-Mead method through the `scipy.optimize` package (Virtanen et al. 2020) to find the optimal  $A$ , mean, and  $\phi_0$  for each sinusoidal model. We show these parameters in Table B1 along with the extrema of the fits, Preston- $r$  value, and reduced  $\chi^2$ .

**Table B1.** Best parameters for the co-sinusoidal ( $A \cos(\phi - \phi_0) + m$ ) fits to the  $\langle B_z \rangle$  measurements of DU2021 and J2021, for the various periods listed in the text. We note that this fit could also correspond to an offset dipole. Additionally, we list the extrema of  $\langle B_z \rangle$  predicted by the fit along with the associated  $r$  value that constrains the relationship between  $i$  and  $\beta$  (Preston 1967). We also list the reduced  $\chi^2$ .

$P$ (d)	Dataset	$A$ (kG)	mean (kG)	$\phi_0$	max	min	$r$	$\chi^2_{\text{red}}$
157.99	DU2021	2.863	3.054	0.627	5.917	0.191	0.032	10.264
157.99	J2021	1.836	1.837	0.586	3.673	0.001	0.000	5.458
153.17	DU2021	2.907	3.082	-0.177	5.988	0.175	0.029	12.088
153.17	J2021	1.818	1.766	-0.056	3.583	-0.052	-0.015	5.233
306.56	DU2021	4.655	0.460	-0.162	5.116	-4.195	-0.820	1.104
306.56	J2021	3.024	0.278	-0.237	3.302	-2.746	-0.832	3.494

## REFERENCES

Astropy Collaboration, Robitaille, T. P., Tollerud, E. J., et al. 2013, *A&A*, 558, A33, doi: [10.1051/0004-6361/201322068](https://doi.org/10.1051/0004-6361/201322068)

Astropy Collaboration, Price-Whelan, A. M., Sipőcz, B. M., et al. 2018, *AJ*, 156, 123, doi: [10.3847/1538-3881/aabc4f](https://doi.org/10.3847/1538-3881/aabc4f)

Astropy Collaboration, Price-Whelan, A. M., Lim, P. L., et al. 2022, *ApJ*, 935, 167, doi: [10.3847/1538-4357/ac7c74](https://doi.org/10.3847/1538-4357/ac7c74)

Babel, J., & Montmerle, T. 1997, *A&A*, 323, 121

Cloutier, R., Doyon, R., Bouchy, F., & Hébrard, G. 2018, *AJ*, 156, 82, doi: [10.3847/1538-3881/aacea9](https://doi.org/10.3847/1538-3881/aacea9)

David-Uraz, A., Petit, V., Shultz, M. E., et al. 2021, *MNRAS*, 501, 2677, doi: [10.1093/mnras/staa3768](https://doi.org/10.1093/mnras/staa3768)

David-Uraz, A., Erba, C., Petit, V., et al. 2019, *MNRAS*, 483, 2814, doi: [10.1093/mnras/sty3227](https://doi.org/10.1093/mnras/sty3227)

Donati, J.-F., Semel, M., Carter, B. D., Rees, D. E., & Collier Cameron, A. 1997, *MNRAS*, 291, 658

Erba, C., David-Uraz, A., Petit, V., et al. 2021, *MNRAS*, 506, 5373, doi: [10.1093/mnras/stab1853](https://doi.org/10.1093/mnras/stab1853)

Grunhut, J. H., Wade, G. A., Neiner, C., et al. 2017, *MNRAS*, 465, 2432, doi: [10.1093/mnras/stw2743](https://doi.org/10.1093/mnras/stw2743)

Horne, J. H., & Baliunas, S. L. 1986, *ApJ*, 302, 757, doi: [10.1086/164037](https://doi.org/10.1086/164037)

Järvinen, S. P., Hubrig, S., Schöller, M., et al. 2021, *MNRAS*, 501, 4534, doi: [10.1093/mnras/staa3919](https://doi.org/10.1093/mnras/staa3919)

Keszthelyi, Z. 2023, *Galaxies*, 11, 40

Lomb, N. R. 1976, *Ap&SS*, 39, 447, doi: [10.1007/BF00648343](https://doi.org/10.1007/BF00648343)

MacInnis, R. 2016, Master's thesis, Department of Physics and Space Sciences, Florida Institute of Technology, Melbourne, Florida, 0

Maíz Apellániz, J., Trigueros Páez, E., Jiménez Martínez, I., et al. 2019a, in *Highlights on Spanish Astrophysics X*, ed. B. Montesinos, A. Asensio Ramos, F. Buitrago, R. Schödel, E. Villaver, S. Pérez-Hoyos, & I. Ordóñez-Etxeberria, 420–420, doi: [10.48550/arXiv.1810.10943](https://doi.org/10.48550/arXiv.1810.10943)

Maíz Apellániz, J., Pellerin, A., Barbá, R. H., et al. 2012, in *Astronomical Society of the Pacific Conference Series*, Vol. 465, *Proceedings of a Scientific Meeting in Honor of Anthony F. J. Moffat*, ed. L. Drissen, C. Robert, N. St-Louis, & A. F. J. Moffat, 484. <https://arxiv.org/abs/1109.1492>

Maíz Apellániz, J., Trigueros Páez, E., Negueruela, I., et al. 2019b, *A&A*, 626, A20, doi: [10.1051/0004-6361/201935359](https://doi.org/10.1051/0004-6361/201935359)

Mathys, G. 2017, *A&A*, 601, A14

Meynet, G., Eggenberger, P., & Maeder, A. 2011, *A&A*, 525, L11

Nazé, Y., Rauw, G., Pollock, A. M. T., Walborn, N. R., & Howarth, I. D. 2007, *MNRAS*, 375, 145, doi: [10.1111/j.1365-2966.2006.11270.x](https://doi.org/10.1111/j.1365-2966.2006.11270.x)

Nazé, Y., Sundqvist, J. O., Fullerton, A. W., et al. 2015, *MNRAS*, 452, 2641, doi: [10.1093/mnras/stv1445](https://doi.org/10.1093/mnras/stv1445)

Negueruela, I., Maíz-Apellániz, J., Simón-Díaz, S., et al. 2015, in Highlights of Spanish Astrophysics VIII, 524–529.  
<https://arxiv.org/abs/1412.5638>

Oksala, M. E., Wade, G. A., Townsend, R. H. D., et al. 2012, MNRAS, 419, 959, doi: [10.1111/j.1365-2966.2011.19753.x](https://doi.org/10.1111/j.1365-2966.2011.19753.x)

Owocki, S. P., ud-Doula, A., Sundqvist, J. O., et al. 2016, MNRAS, 462, 3830, doi: [10.1093/mnras/stw1894](https://doi.org/10.1093/mnras/stw1894)

Petit, P., Louge, T., Théado, S., et al. 2014, PASP, 126, 469, doi: [10.1086/676976](https://doi.org/10.1086/676976)

Petit, V., Cohen, D. H., Wade, G. A., et al. 2015, MNRAS, 453, 3288, doi: [10.1093/mnras/stv1741](https://doi.org/10.1093/mnras/stv1741)

Petit, V., Keszthelyi, Z., MacInnis, R., et al. 2017, MNRAS, 466, 1052, doi: [10.1093/mnras/stw3126](https://doi.org/10.1093/mnras/stw3126)

Preston, G. W. 1967, ApJ, 150, 547, doi: [10.1086/149358](https://doi.org/10.1086/149358)

Scargle, J. D. 1982, ApJ, 263, 835, doi: [10.1086/160554](https://doi.org/10.1086/160554)

Shenar, T., Wade, G. A., Marchant, P., et al. 2023, Science, 381, 761, doi: [10.1126/science.adc3293](https://doi.org/10.1126/science.adc3293)

Simón-Díaz, S., Pérez Prieto, J. A., Holgado, G., de Burgos, A., & Iacob Team. 2020, in Contributions to the XIV.0 Scientific Meeting (virtual) of the Spanish Astronomical Society, 187

Simón-Díaz, S., Negueruela, I., Maíz Apellániz, J., et al. 2015, in Highlights of Spanish Astrophysics VIII, 576–581.  
<https://arxiv.org/abs/1504.04257>

Stahl, O., Wade, G., Petit, V., Stober, B., & Schanne, L. 2008, A&A, 487, 323, doi: [10.1051/0004-6361:200809935](https://doi.org/10.1051/0004-6361:200809935)

Stibbs, D. W. N. 1950, MNRAS, 110, 395, doi: [10.1093/mnras/110.4.395](https://doi.org/10.1093/mnras/110.4.395)

Sundqvist, J. O., Puls, J., & Owocki, S. P. 2014, A&A, 568, A59, doi: [10.1051/0004-6361/201423570](https://doi.org/10.1051/0004-6361/201423570)

ud-Doula, A., Owocki, S., Townsend, R., Petit, V., & Cohen, D. 2014, MNRAS, 441, 3600, doi: [10.1093/mnras/stu769](https://doi.org/10.1093/mnras/stu769)

ud-Doula, A., & Owocki, S. P. 2002, ApJ, 576, 413, doi: [10.1086/341543](https://doi.org/10.1086/341543)

ud-Doula, A., Owocki, S. P., & Townsend, R. H. D. 2008, MNRAS, 385, 97, doi: [10.1111/j.1365-2966.2008.12840.x](https://doi.org/10.1111/j.1365-2966.2008.12840.x)

—. 2009, MNRAS, 392, 1022, doi: [10.1111/j.1365-2966.2008.14134.x](https://doi.org/10.1111/j.1365-2966.2008.14134.x)

ud-Doula, A., Sundqvist, J. O., Owocki, S. P., Petit, V., & Townsend, R. H. D. 2013, MNRAS, 428, 2723, doi: [10.1093/mnras/sts246](https://doi.org/10.1093/mnras/sts246)

VanderPlas, J. T. 2018, ApJS, 236, 16, doi: [10.3847/1538-4365/aab766](https://doi.org/10.3847/1538-4365/aab766)

Virtanen, P., Gommers, R., Oliphant, T. E., et al. 2020, Nature Methods, 17, 261, doi: [10.1038/s41592-019-0686-2](https://doi.org/10.1038/s41592-019-0686-2)

Wade, G. A., Maíz Apellániz, J., Martins, F., et al. 2012a, MNRAS, 425, 1278, doi: [10.1111/j.1365-2966.2012.21523.x](https://doi.org/10.1111/j.1365-2966.2012.21523.x)

Wade, G. A., Grunhut, J., Gräfener, G., et al. 2012b, MNRAS, 419, 2459, doi: [10.1111/j.1365-2966.2011.19897.x](https://doi.org/10.1111/j.1365-2966.2011.19897.x)

Wiese, W. L. 2000, in American Institute of Physics Conference Series, Vol. 543, Atomic and Molecular Data and their Applications, ICAMDATA, ed. K. A. Berrington & K. L. Bell, 299–303, doi: [10.1063/1.1336287](https://doi.org/10.1063/1.1336287)